# Secondary dispersal of seagrass seeds in complex micro-topographies.

A. Alvarez,

Department of Marine Ecology (MARE), Instituto Mediterraneo de Estudios Avanzados-IMEDEA (CSIC-UIB), C/ Miquel Marques 21, 07190 Esporlas, Spain, e-mail: alberto.alvarez@imedea.uib-csic.es

## Abstract

Motivated by observational and experimental evidence, a theoretical model is proposed to relate the secondary dispersal of seagrass seeds with the complexity of micro-topography in natural environments. Complexity is encoded in terms of the Hurst exponent of a fractal description of the micro-topographical geometry. The percentage of a seafloor transect where secondary dispersal of seagrass seeds occurs, is quantified in terms of the mainstream velocity, bottom complexity and properties of the seeds. Theoretical expressions are validated considering the cases of *Zostera marina* and *Posidonia oceanica* seeds and using computational fluid dynamics (CFD). A total of 200 CFD simulations with different bottom complexities and flow conditions, were done for each seagrass genus to validate the theoretical model. Numerical results agree with theoretical predictions. This finding provides a guideline to artificially adapt seafloor roughness in seed-based restoration areas to control secondary dispersal of seeds.

**Keywords:** seagrass meadows; seed dispersal; micro-topography; fractals; computational fluid dynamics.

## 1. Introduction

Seagrasses are marine aquatic angiosperm widely distributed through the coastal regions across the globe (Orth et al., 2006a). Seagrass meadows are ecologically important because they constitute the habitat of diverse species (Duffy, 2006; Heck et al., 2008) and improve the water quality conditions in coastal regions (Denninson et al., 1993; McGlathery et al., 2007). Moreover, it has been hypothesized that they can represent an important carbon sink (Duarte et al., 2005; Fourqurean et al., 2012) and nitrogen removal (Zarnoch et al., 2017) in marine areas. Unfortunately, anthropogenic disturbances in the coastal environments have resulted in a reduction of seagrass populations (Duarte, 2002; Orth et al., 2006a; Waycott et al., 2009). Understanding the different aspects of the ecological dynamics of the seagrass meadows, is required for their present and future preservation.

Dispersal is a determinant aspect of the ecological and evolutionary processes in seagrass meadows (Orth et al., 2006b). In particular, seed dispersal shapes their distribution, structure and resilience (Les et al., 2003). Two phases characterize the dispersal of seagrass seeds: the primary dispersal refers to the movement of the seed from the parent plant to the sediment surface. Transport by water currents seems to be the dominant primary dispersal mechanism of seagrass seeds (MacMahon et al., 2014). A long-distance dispersal results in this phase when seeds are positive buoyant or the movement is mediated through rafting on the water surface of spathes, flowering branches (rhipidia) and reproductive shoots (Harwell and Orth, 2002; Kallstrom et al., 2008; Kendrick et al., 2012; McMahon et al., 2014; Hosokawa et al., 2015). Observational evidence suggests that the primary dispersal distances of seagrass seeds of as much as 150 km, are possible (Harwell and Orth, 2002; Olsen et al., 2004; Kallstrom et al., 2008). Instead, a short distance primary dispersal around the parent population occurs in seagrass genera producing negative buoyant seeds (Orth et al., 1994).

The movement from the initial point of settlement to other location is known as secondary dispersal. This mobilization of negatively buoyant seeds from the sediment, occurs through abiotic processes (currents, waves, sediment movement) (Orth et al., 1994) and/or biotic vectors (Orth et al., 2000). However, hydrodynamically-mediated transport seems to be the dominant mobility mechanism at the seafloor (Marion and Orth, 2010). To this regard, the relationship between secondary dispersal and hydrodynamic conditions at the seafloor needs further research (Koch et al., 2010; Ruiz-Montoya et al., 2012).

The transport of negatively buoyant seeds as bedload, occurs when the shear stress at the seabed exceed some critical threshold (named as critical erosion shear stress or Shields parameter when it is dimensionless (Ternat et al., 2008)). The bottom shear stress is a function of the currents, the grain size and the micro-topographic features such as sand ripples or bioturbation structures (Ackerman and Hoover, 2001; Jumars and Nowell, 1984). Regarding the latter, observational and flume studies found that small bottom surface irregularities appear to be accumulation sites for the seagrass seeds. Orth et al. (1994) consistently observed patterns of *Zostera marina* seeds trapping within a region of deposition, despite the existence of hydrodynamic conditions favorable for their transport. These authors suggested that micro-topography reliefs on the seafloor armored seeds from ambient flow. Luckenbach and Orth (1999) observed in flume experiments, the retention of *Z. marina* seeds by micro-topographic reliefs generated by benthic invertebrates. Seeds which should be widely disperse as bedload were trap even by small non-uniformities at the seafloor. Inglis (2000) also evidenced that deposition of seeds of *Halodule uninervis* occurred in greatest abundance in the troughs of small sand waves and in the trails excavated by dugongs. Balestri et al. (2017) analysed published and unpublished data of recruitment of *Posidonia oceanica* to examine, among other factors, the habitat characteristics at recruitment sites. The authors discovered that recruitment on rocky habitats was twofold more than on sandy substrates. Pereda-Briones et al. (2018) found in flume experiments that complex substrata, are more capable of retaining different seagrass seeds. These observations and flume experiments suggest an important correlation between the complexity of the micro-topography and the dispersal and colonization of habitats by seagrasses. Mathematical formalization of this relationship would contribute to further understand the ecological implications of secondary dispersal, as well as it could have practical applications in seed-based restoration where secondary dispersal is a limiting factor (Marion and Orth, 2010).

Micro-topography refers to the scale of roughness concerned with small-scale sedimentary structures such as pebble clusters, transverse ribs, pits, mounds, burrows etc. (Robert, 1991). In terms of flow resistance processes, the distribution of sizes and shapes of these micro-topographic features increases the energy loss of the flow. Characterizing the hierarchy of roughness elements of the micro-topography, remains an important difficulty. Experimental quantification of small-scale bottom features has been attempted with high-resolution sonar mapping systems, stereo photogrammetry and micro-topographic laser scanners (Briggs, 1989; Lyons and Pouliquen, 2004; Du Preez and Tunnicliffe, 2012). Still, the lack of a robust approach to characterize *in situ* the seafloor micro-topography is repeatedly cited as a source of uncertainty in derived analysis (Lyons and Pouliquen, 2004).

Micro-topography often demonstrates self-similar fractal-like properties (Fox and Hayes, 1985). For this reason, fractal analysis has provided a particularly fruitful methodology to characterize the complexity of roughness (Xu et al., 1993; Smith, 2014). A scaling parameter in fractals known as the Hurst exponent (H), is of special interest for the present study. An increase of a factor $r$ in the horizontal scales, corresponds to an increment of the vertical scales by a factor $r^H$. Since horizontal scales at the seafloor increases more rapidly than vertical lengths, $0 \leq H \leq 1$. The fractal dimension of a profile (D) is related to the Hurst exponent, by the relationship D=2-H (Smith, 2014). Thus, decreasing H increases the degree of roughness of a fractal profile. Moreover, the power spectrum of a fractal profile, $\beta$, is also related to H by $\beta$=2H+1. The use of a power law form to characterize bottom roughness over a wide range of spatial frequencies, is a useful and popular method (Fox and Hayes, 1985; Lyons et al., 2002). Even though the seafloor is continually changing, the previous statistical description is assumed to be relatively stable (Lyons and Pouliquen, 2004).

Motivated by the experimental findings previously described and by its potential practical applications, this article explores the relationship between the secondary dispersal of seagrass seeds by currents and the complexity of micro-topographic profiles. Specifically, the present objective is to quantify in terms of the Hurst exponent and flow conditions, the cumulative length in a fractal micro-topographic profile where secondary dispersal of seagrass seeds occurs. A simple theoretical framework is first developed to derive general scaling dependences for practical use. Theoretical expressions are then validated using numerical techniques from computational fluid dynamics (CFD). Specifically, the conditions for secondary dispersal of seeds of *Z. marina* and *P. oceanica* on micro-topographic profiles are simulated for different fractal dimensions of the bottom profile and flow conditions. The paper is organized as follows: Section 2 present the theoretical development while details about the numerical fluid model are described in Section 3. Results are reported and discussed in Sections 4 and 5, respectively.

## 2. Methods

### 2.1 Theoretical method

An analytic treatment is proposed here to provide simple predictive expressions to estimate the portion of a complex micro-topographic transect, where secondary dispersal of seeds occurs. The analytical approach starts considering an isolated roughness element placed in a flow channel with a smooth bottom. The bottom shear stress, $\tau_B$, at the element is partitioned into two components (Einstein and Banks, 1950):

$$\tau_B = \tau_F + \tau_S \quad (1)$$

Where $\tau_F$ and $\tau_S$ are the form and the skin friction shear stresses, respectively. The former results from pressure differences due to local flow separation and re-circulation in the lee region of the roughness element. These pressure gradients are normal to the surface and thus the form drag shear stress has no impact on the bedload transport. The latter, results from the skin friction of the water and the bed floor and it is the responsible of the transport of the bed sediments.

An effective reduction of the skin friction shear stress, is expected at the lee of the roughness element as a result of its wake. Its average value over the length of the roughness element, $\bar{\tau}_S$, is expected to be attenuated according:

$$\bar{\tau}_S = \tau_o \theta \quad (2)$$

Where $\tau_o$ is the unperturbed skin friction shear stress in similar flow conditions. $\tau_o$ is assumed to exceed the critical value $\tau_c$ to initiate the motion of the seeds and thus, secondary dispersal of seeds would occur in the entire bottom transect if unperturbed. $\theta$ is a dimensionless parameter smaller than one, that is related to an effective unsheltered length of the roughness element. For a rough bottom constituted by a streamwise array of roughness elements with similar morphology, the resulting skin friction shear stresses at the *n-th* element can be approximated by superimposing *n* individual bottom stresses (Raupach, 1992; Raupach et al., 1993):

$$\bar{\tau}_S = \tau_o \theta^n \qquad (3)$$

According to Eq. (3), $\bar{\tau}_S$ equals the critical value $\tau_c$ after $n_c$ roughness elements, with $n_c$ verifying:

$$\bar{\tau}_S = \tau_c = \tau_o \theta^{n_c} \qquad (4)$$

or,

$$n_c = \frac{1}{\gamma} \ln\left(\frac{\tau_o}{\tau_c}\right) \qquad (5)$$

Where $\gamma$=-In($\theta$) is a positive constant ($\theta$<1). No movement of seeds would be expected after a streamwise distance $L_c=n_c l^*$ over the rough bottom, where $l^*$ is the characteristic length of the roughness element. The length of the transect in which the skin friction shear stress exceeds the critical value can then be estimated as $L_S=\theta L_c$. Using Eq.(5):

$$\frac{L_S}{L} = \frac{n_c\, l^* \theta}{L} = \frac{\theta}{\gamma}\frac{l^*}{L}\ln\left(\frac{\tau_o}{\tau_c}\right) = \frac{2e^{-\gamma}}{\gamma}\frac{l^*}{L}\ln\left(\frac{U_o}{U_c}\right) \qquad (6)$$

Where $U_o$ is the actual free stream velocity and $U_c$ corresponds to the free stream velocity that induces a bottom stress $\tau_c$ in the unperturbed transect. The last term in Eq. (6) is derived from the relationship $\tau_{o,c} = \frac{1}{2}\rho C_f U_{o,c}^2$, where $\rho$ and $C_f$ are the density of the fluid and the skin friction coefficient of the smooth bottom, respectively. In a fractal bottom transect, a characteristic length of the roughness relief ($l^*$) is provided by the correlation length, which is estimated by the ratio between the length of the transect (L) and number (N) of random reliefs (Rees and Arnold, 2006). Statistically, N corresponds to the number of positive zero crossings in the transect (Munro, 1989). In terms of the Hurst exponent, the parameters above follow the relationships (Church, 1988):

$$L = N\, l^*;\; N = \frac{(4H+1)}{2H^2};\frac{l^*}{L} = \frac{2H^2}{(4H+1)} \qquad (7)$$

In this analytical framework, Eqs.(6) and (7) provide an estimate of the cumulative length of the transect with secondary dispersion, $L_s/L$, in terms of the free stream velocity ($U_o$), the characteristics of the roughness elements (H) and the conditions for secondary dispersal of the seeds ($U_c$).

## 2.2 Numerical method

A numerical model has been developed to test the theoretical predictive expressions obtained in the previous Section. To do that, the flow over a rough bottom is simulated in a flume two dimensional section of 0.5 m height and 1.2 m long. Assuming a mainstream symmetry is common in flume studies, because cross flows are negligible with respect to the mainstream. While this assumption captures the major features of the physical processes involved, it significantly reduces the computational efforts. With suitable boundary conditions (detailed later), the domain represents a portion of an open flume arbitrarily long and deep enough to disregard the effects of a free surface. The rough bottom is 1 m long and it is located at the center of the flume, 0.1 m apart from the inflow and outflow boundaries. Realizations of fractal micro-topographies, were generated as one dimensional fractional Brownian motions with Hurst parameters of 0.2, 0.4, 0.5, 0.6 and 0.8 (Figure 1). Despite to the scarce data, diverse observational and experimental studies have characterized the root mean square (rms) height roughness of the micro-topography with values as high as 0.03 m (Briggs, 1989; Wiberg and Harris, 1994; Inglis, 2000; Lyons et al., 2002; Guillen et al., 2008). Accordingly, the rms height ($h$) of each profile was fixed to 0.03 m.

Numerical simulations are particularized for the seeds of *Z. marina* and *P. oceanica*, which are marine aquatic angiosperm widely distributed through the coastal regions of the Northern Hemisphere (Short and Moore, 2006). The former represents a case where seeds are easily transported as bedload (Luckenbach and Orth, 1999), while the latter exemplifies a case where the secondary dispersal of seeds by usual ambient flows is rather limited (Pereda-Briones et al., 2018). Specifically, the critical shear velocity, $u^*_c$ ($u_c^* = \sqrt{\frac{\tau_c}{\rho}}$ where $\tau_c$ y $\rho$ are the critical bottom shear stress and the fluid density, respectively), to initiate the motion of *Z. marina* seeds on a smooth sand bed is $u^*_c$=0.007 m/s, which resulted from a critical free stream velocity of $U_c$=0.1 m/s (Orth et al., 1994). Free stream velocities $U_o$, of 0.15 m/s, 0.2 m/s, 0.25 m/s and 0.3 m/s were considered in the simulations. This range of speeds are typical for the locations where Pereda-Briones et al. (2018) collected *Z. marina* seeds. The transport of *P. oceanica* seeds as bedload is significatively harder than for the *Z. marina* seeds. A critical free stream velocity of $U_c$=0.2 m/s is required to initiate the motion of *P. oceanica* seeds on a smooth sand (Pereda-Briones et al., 2018). For this reason, free stream velocities $U_o$, of 0.25 m/s, 0.3 m/s, 0.35 m/s and 0.4 m/s were considered in this case.

A Reynolds Average Navier–Stokes (RANS) approach along with a turbulence model have been considered for the numerical simulations. Mathematically, the steady RANS model is described by the equations:

$$\frac{\partial(U_i U_j)}{\partial x_j} = -\frac{1}{\rho}\frac{\partial P}{\partial x_i} + (\nu + \nu_T)\frac{\partial^2 U_i}{\partial x_j \partial x_j} \qquad (8)$$

$$\frac{\partial U_i}{\partial x_i} = 0 \qquad (9)$$

where $U_i$ is the *i-th* component of the time averaged velocity, $\rho$ is the density, *P* is the pressure and $\nu$ is the kinematic viscosity ($10^{-6}$ $m^2/s$). The Einstein summation convention is assumed for repeated indices. The eddy viscosity $\nu_T$ which parametrizes the dispersal effect of the small scales onto the large scales, is computed with the Baldwin-Lomax eddy viscosity model (Baldwin and Lomax, 1978; Wilcox, 1993; Appendix 1). This model is widely employed for its ease of implementation and robustness. It faithfully reproduces friction velocity and velocity profiles for incompressible turbulent boundary layers, providing reasonable accuracy for steady flows with no or mild separation (Willcox, 1993). The latter is the situation expected in the present study.

The system of Equations (8) - (9) is solved with the following boundary conditions:

$$
\begin{array}{ll}
U = U(y), V = 0, \ \mathbf{n}.\nabla P = 0 & \text{Inflow boundary} \\
\mathbf{n}.\nabla U = \mathbf{n}.\nabla V = 0, P = 0 & \text{Outflow boundary} \\
\mathbf{n}.\nabla U = \mathbf{n}.\nabla V = \mathbf{n}.\nabla P = 0 & \text{Top boundary} \\
U = V = \mathbf{n}.\nabla P = 0 & \text{Bottom boundary}
\end{array}
$$

where **n** is the vector normal to the boundary. A logarithmic inlet velocity profile with components $U(y) = u^*_e$ In $(9.793\ y\ u^*_e /\nu)/K$ (where $u^*_e$ is a theoretical estimate of the friction velocity $u^*$ based on the freestream velocity and K=0.4 is the von Karman's constant) and V=0 is prescribed at the left boundary. This inflow condition facilitates the convergence of the numerical algorithm. The outflow boundary condition is of the do-nothing type (Gresho, 1991), allowing the fluid to cross the boundary in either direction to preserve continuity. Slip and non-slip boundary conditions are prescribed for the velocity field at the top and bottom boundaries, respectively. This type of boundary conditions allows us to consider the computational domain as part of a larger open flume.

A standard Galerkin finite element method based on the triangular Taylor-Hood element (Taylor and Hood, 1973), has been employed for the spatial discretization of Equations (8)-(9). In the Taylor-Hood element, pressure and velocity nodes are located at the vertices and at the vertices and middle-edge points of the triangular element, respectively. Thus, the velocity and pressure discrete approximations are both piecewise continuous, the former being quadratic and the latter linear (Donea and Huerta, 2003). The Taylor-Hood elements are stable in that they fulfill the inf-sup compatibility condition (a condition that discrete spaces must satisfy to guarantee the stability of the results, Brezzi and Bathe, 1990). They also exhibit optimal quadratic convergence (Donea and Huerta, 2003). For these reasons, the Taylor-Hood finite element is the standard finite element for simulating incompressible fluid flow (Larson and Bengzon, 2013).

A Picard iteration technique was used to solve the nonlinear equations resulting after the spatial discretization. Starting with an initial guess for the velocity field, Picard's method constructs a sequence of approximate solutions $\left(\vec{U}^{k+1}, P^{k+1}\right)$ by solving at each iteration the linear Oseen problem (Rhebergen et al., 2013):

$$\frac{\partial\left(U_i^{k+1}U_j^k\right)}{\partial x_j} + \frac{1}{\rho}\frac{\partial P^{k+1}}{\partial x_i} - \left(\nu + \nu_T^k\right)\frac{\partial U_i^{k+1}}{\partial x_j \partial x_j} = g_i \qquad (10)$$

$$\frac{\partial U_i^{k+1}}{\partial x_i} = 0 \qquad (11)$$

Where superscript *k*=1,2… in the model variables refers to the solution at the *k-th* iteration. $g_i$ collects the boundary forcing terms prescribed by the inflow and boundary conditions. The convergence criterion used in this work to stop the iteration process is:

$$\frac{\|\vec{U}^{k+1} - \vec{U}^k\|}{\|\vec{U}^k\|} < 10^{-3} \qquad (12)$$

This convergence criterion resulted on a good compromise between accuracy and computational cost.

An adaptive mesh which is refined in the vicinity of the bottom boundary, was constructed in order to capture fine features of the flow. The domain geometry was tessellated into 26331 triangular elements with characteristic sizes ranging from $1.5 \times 10^{-4}$ m at the seafloor up to $2 \times 10^{-2}$ m at the upper boundary (Figure 2). Regarding the resolution of the roughness elements, more than 10 grid points resolve the roughness in wall-normal and streamwise directions. It has also been verified that the mesh is dense enough to resolve the structure of the boundary layer (see below).

The computational methodology to generate fractal profiles of the seafloor has been detailed in previous articles (Kroese and Botev, 2015), to which interested readers are referred for further information.

## 3 Results

A numerical simulation was initially done considering a smooth bottom, to validate the numerical implementation as well as the suitability of the mesh resolution. The structure of the turbulent boundary layer of a viscous flow close to a smooth wall is well known from scaling considerations (Wilcox, 1993). Briefly, three distinct regions are observed namely viscous sublayer, log layer and defect layer. Only the first two regions are relevant for this study. The viscous sublayer is the closest to the wall ($y^+<11$ where $y^+ = y\, u^*/\nu$ is the dimensionless distance from the wall in wall coordinates) and the flow dynamics is mainly controlled by viscous forces. The dimensionless velocity $U^+=U/u^*$ and distance to the wall $y^+$ follows the relation $U^+=y^+$ in this sublayer. The log layer ($25<y^+<1000$) is found after the viscous sublayer. The dynamics is mainly dictated by nonlinear interactions and the average turbulent velocity at a particular point is proportional to the logarithm of the distance of the point under consideration from the wall, $U^+=\text{In}(9.793\ y^+)/K$.

Figure 3 displays the structure of the boundary layer in the numerical channel, obtained from an inflow with a free stream velocity of $U_o$=0.2 m/s. Results evidence that the numerical model nicely reproduces the expected structure of the turbulent boundary layer. Further comparison between the numerical results and the theory is done in Figure 4. Specifically, the Figure compares the theoretical vertical profile of $U^+$ with the numerical one in a station at the middle of the channel. Again, a good agreement is found with the theoretical profile at the viscous sublayer and log layer. Notice the existence of a transition region between both layers, $11<y^+<20$, where theoretical scaling arguments are not applicable. The Figure also compares the inflow profile introduced as boundary condition, with the theoretical profile corresponding to the structure of the turbulent boundary layer. This comparison reveals that the inflow boundary condition is well adjusted to the correct scaling in the external log layer. Conversely, the inflow profile significantly differs from the correct one in the viscous sublayer.

A total of 200 numerical simulations with the CFD model considering different fractal bottom profiles and free stream velocities, were done for each seagrass genus to validate the theoretical model. Specifically, an ensemble of 10 random realizations of micro-topographic profiles were considered for each Hurst exponent (H) and free stream velocity ($U_o$). For each realization, the bottom friction velocity, $u^*(x)$, was numerically computed along the bottom profile and the cumulative length ($L_S$) of the regions where $u^*(x) > u_c$, calculated. Finally, the cumulative length for secondary dispersal of *Z. marina* seeds for a given H and $U_o$, was obtained as the ensemble average $<L_S>$ of the cumulative lengths of the individual realizations. Figure 5 displays the relationship between $\langle L_S \rangle/L$ and $l^* In(U_o/U_c)/L$ obtained for the considered values of H and $U_o$ and each seagrass genus. A straight line with a slope of 2.67 and a regression coefficient of 0.983, results from the linear fit of the data points for the *Z. marina*. A value of $\theta$=0.754 is derived from this linear fit. For the case of the *P. oceanica*, the slope and regression coefficients are 2.77 and 0.986, respectively, with a value of $\theta$=0.760. Finally, a slope of 2.69, a correlation coefficient of 0.984 and a $\theta$ value of 0.755 results from the linear fitting of the data regardless of the seagrass genus. The latter fit is displayed in Figure 5. Numerical results confirm the validity of the relationship Eq. (6) obtained from the analytical study.

## 4 Discussion

This study provides a quantification of the role of micro-topography in the secondary dispersal of seagrass seeds. An estimate of the portion of a rough bottom where secondary dispersal occurs was obtained based on fundamental arguments. Specifically, two physical assumptions are considered when developing the theory. The first hypothesis considers the partition of the total shear stress between that arising from pressure differences over and around roughness elements (form drag) and the frictional drag on the intervening surface. While a wide consensus exists on the arithmetic partition of the total shear stress, different methodologies have been suggested to estimate its components in terms of the flow conditions and bottom properties (interested readers are referred to Le Bouteiller and Venditti, (2015) for a concise review). To this regard, a second hypothesis considers that the average frictional stress over a roughness element, is expected to be smaller than the unobstructed stress $\tau_o$. This results from the negligible contribution to the skin friction of the front and rear separation zones or the standing eddies, located on the roughness element. Moreover, the attenuation coefficient (θ) is assumed independent of the characteristic length of the roughness element ($l^*$). This situation is expected if roughness elements are significantly embedded in the wakes of its neighbors. Experiments and numerical simulations evidence that at high Reynolds numbers, the turbulent boundary layer reattaches at a distance of about 6*h* after bedforms of characteristic height *h* (Nelson and Smith, 1989). Thus, the independence of θ with $l^*$ would suggest that $l^*$ is less or of the same order than 6h. Briggs (1989) provides some observational evidence that this could be the case for relatively rough micro-topography. This author measured a correlation length of 0.085 m in a rough bottom with rms height (h) of 0.025 m. This condition also holds in most of the fractal descriptions of the micro-topography used in the simulations and derived from seafloor parameters reported in observations. Nevertheless, no observational nor experimental study has yet addressed how general this condition is in natural environments.

Theoretical results have been compared against numerical simulations of different flow regimes over fractal micro-topographies. Numerical results agree with theoretical expectations. Specifically, the ensemble average length where secondary dispersal occurs in a fractal micro-topography, was found linearly related with the product of the characteristic length of the roughness elements times the logarithm of the ratio between the free stream and critical velocities. As expected from the theory, a similar value of the attenuation coefficient θ of about 0.75 has been numerically obtained for both cases of *Z. marina* and *P. oceanica*. This value can be intuitively understood considering that conditions for secondary dispersal statistically occurs at the exposed front part of the roughness element. Moreover, the result also confirms the independence of θ with $l^*$. To this regard, CFD simulations have been revealed as a useful tool to test theoretical arguments in virtual physical environments complex enough to represent the physical processes of interest, but simple enough to facilitate statistical inferences. Certainly, numerical modelling technologies cannot fully represent reality and thus, present results encourage their future experimental and observational confirmation.

Theoretical and numerical results contribute to clarify and quantify the role of micro-topography in the entrapment of seagrass seeds in natural environments. Observational evidence supports the hypothesis that the secondary dispersal of these seeds is limited to the immediate vicinity of seed release. This limited secondary dispersal may be interpreted in terms of the micro-topography complexity. Vegetation significantly attenuate the capability of the ambient flow to disperse seeds that fall within the seagrass meadow (Orth et al., 1994). Moreover, a high micro-topography complexity (low Hurst exponent) is expected inside the seagrass meadows, due to secondary flows resulting from the interaction of the mainstream with the body of the plant as well as due to plant litter. The micro-topography is expected to play a more significant role in the secondary dispersal of seeds that land within open vegetation or exposed soils. Significant seed accumulations can be found in these regions even with supercritical flows if small-scale disturbances are present (Orth et al., 1994; Inglis, 2000).

Seeds can be an important mechanism to successfully restore large areas of seagrass coverage (Pickerell et al., 2005; Orth et al., 2006c). For seagrass species producing abundant and easy-to-harvest seeds, seed-based restoration introduces significant technological and economic advantages versus restoration techniques relying on adult plants, (Marion and Orth, 2010). However, low initial seedling establishment rates have been recognized as a major limitation for seed-based restoration projects (Marion and Orth, 2010). Seed retention and seedling establishment can be facilitated by artificially adapting seafloor roughness. Natural or artificial roughness elements could be used, to engineer appropriate mulches to trap naturally dispersed seeds and to enhance seed retention. Present results provide a guideline to determine, a priori, the required complexity of the micro-topographical mulch to satisfy, given seed properties and expected environmental conditions, a desired degree of seed retention in the habitat to be restored.

The findings of the present work could also be applied, with certain caution, to land systems. This will work when wind is the dominant dispersal agent. Observations also evidence that wind-blown seeds in land systems, are more easily trapped on rough soils than on smooth ones (Johnson and Fryer, 1992; Chambers and MacMahon, 1994). This study provides a physical foundation for these observations. Notice, however, that secondary dispersal of seeds in land systems often results from overland flows generated by intense precipitations (Chambers and MacMahon, 1994). Although being a hydrodynamically-mediated transport of seeds, present findings are not directly applicable to this case. The proximity of the air-water interface to the soil and the usual high speeds of overland flows, may invalidate some of the assumptions considered in the theory.

To conclude, this study has proposed and numerically validated a link between the small-scale properties of micro-topography (H or $l^*$) and the global bed characteristics ($<L_S>$) for secondary dispersal of seagrass. Although there are some observational and/or experimental evidences that would support the results, their confirmation by dedicated observations and/or experiments still remains open. The proposed relationship constitutes a valuable tool to understand the dispersal and colonization of habitats by seagrasses. To this regard, it provides the physical explanation to observational evidence. It could also support seed-based restoration techniques.

## References


Ackerman, J. D., Hoover, T. 2001. Measurement of local bed shear stress in streams using a Preston-static tube. *Limmol. Oceanogr.*, 46, 2080-2087.

Baldwin, B. S., Lomax, H. 1978. Thin Layer Approximation and Algebraic Model for Separated Turbulent Flows, *AIAA*, 78-257.

Balestri, E., Vallerini, F., Lardicci, C. 2017. Recruitment and patch establishment by seed in the seagrass Posidonia oceanica: Importance and conservation implications. *Front. Plant Sci.*, 8, 1067.

Brezzi, F., Bathe, K. J. 1990. A discourse on the stability conditions for mixed finite element formulations. *Comp. Methods Appl. Mech. Eng.*, 82, 27-57.

Briggs, K. B. 1989. Microtopographical roughness of shallow water continental shelves. *IEEE J. Ocean. Eng.*, 14, 360-367.

Chambers, J. C., MacMahon, J. A. 1994. A day in the life of a seed: movements and fates of seeds and their implications for natural and managed systems. *Ann. Rev. Ecol. Sys.*, 25, 263-292.

Church, L. E. 1988. Fractal surface finish. *Appl. Opt.*, 27, 1518-1526.

Denninson, W. C., Orth, R. J., Moore, K. A., Stevenson, J. C., Carter, V., Kollar, S. *et al.* 1993. Assessing water quality with submersed aquatic vegetation: Habitat requirements as barometers of Chesapeake Bay health. *Bioscience*, 43, 86-94.

Donea J., Huerta A. 2003. *Finite element methods for flow problems*. Wiley and Sons Ltd., Chichester, West Sussex, UK, pp. 350.

Duarte, C. M. 2002. The future of seagrass meadows. *Environ Conserv.*, 29, 192–206.

Duarte, C. M., Middelburg, J., Caraco, N. 2005. Major role of marine vegetation on the oceanic carbon cycle. *Biogeoscience*, 2,1– 8.

Duffy, J. E. 2006. Biodiversity and the functioning of seagrass ecosystems. *Mar. Ecol. Prog. Ser.*, 311, 233–250.

Du Preez, C., Tunnicliffe, V. 2012. A new video survey method of microtopographic laser scanning (MiLS) to measure small-scale seafloor bottom roughness. *Limnol. Oceanogr.: Methods*, 10, 899–909.

Einstein, H., A., Banks, R. B., 1950. Fluid resistence of composited roughness. *Trans. AGU*, 31, 603-610.

Fourqurean, J. W., Duarte, C. M., Kennedy, H., Marba, N., Holmer, M., Mateo, M. A., Apostolaki, E. T., Kendrick, G. A., Krause-Jensen, D., McGlathery, K. J., 2012. Seagrass ecosystems as a globally significant carbon stock. *Nat. Geosci*., 5, 505-509.

Fox, C. G., Hayes, D. E., 1985. Quantitative methods for analyzing the roughness of the seafloor. *Rev. Geophys.*, 23, 1-48.

Gresho, P. M., 1991. Some current CFD issues relevant to the incompressible Navier-Stokes equations. *Comput. Methods Appl. Mech. Eng.*, 87, 201–252.

Guillén, J., Soriano, S., Demestre, M., Falqués, A., Palanques, A., Puig, P., 2008. Alteration of bottom roughness by benthic organisms in a sandy coastal environment. *Cont. Shelf Res.*,28, 2382-2392,

Harwell, M. C., Orth, R. J., 2002. Long-distance dispersal potential in a marine macrophyte. *Ecol.*, 83, 3319-3330.

Heck Jr., K. L., Carruthers, T. J. B., Duarte, C. M., Hughes, A. R., Kendrick, G., Orth, R. J., Williams, S. W., 2008. Trophic transfers from seagrass meadows subsidize diverse marine and terrestrial consumers. *Ecosystems*, 11, 1198-1210.

Hosokawa, S., Nakaoka, M., Miyoshi, E., Kuwae, T., 2015. Seed dispersal in the seagrass *Zostera marina* is mostly within the parent bed in a protected bay. *Mar. Ecol. Prog. Ser.*, 523, 41-56.

Inglis, G. J.,2000. Disturbance-related heterogeneity in the seed banks of a marine angiosperm. *J. Ecol.*, 88, 88–99.

Johnson, E. A., Fryer, G. I., 1992. Physical characterization of seed microsites-movement on the ground. *J. Ecol.*, 80, 823-836.

Jumars, P. A., Nowell, A. R., 1984. Effects of benthos on sediment transport: difficulties with functional grouping. *Cont. Shelf Res.*, 3, 115-130.

Kalstrom B., Nyqvist, A., Aberg, P. Bodin, M, André, C., 2008. Seed rafting as a dispersal strategy for eelgrass (*Zostera marina*). *Aquat. Bot.*, 88, 148-153.

Kendrick, G. A., Waycott, M., Carruthers, T. J. B., Cambridge, M. L. and others, 2012. The central role of dispersal in the maintenance and persistence of seagrass populations. *Bioscience*, 62, 56-65.

Koch, E. W., Ailstock, M. S., Booth, D. M., Shafer, D. J., Magoun, A. D., 2010. The role of currents and waves in the dispersal of submersed angiosperm and seedlings. *Restor. Ecol.*, 18, 584-595.

Kroese, D. P., Botev, Z. I., 2015. Spatial Process Simulation. In: *Stochastic Geometry, Spatial Statistics and Random Fields*, ed. Schmidt, V. Springer, Cham, pp. 369-404.

Larson, M. G., Bengzon, F., 2013. *The finite element method: Theory, implementations and applications*. Springer, Heidelberg, pp. 385.

Le Boutieller, G., Venditti, J. G., 2015. Sediment transport and shear stress partitioning in a vegetated flow. *Water Resour. Res.*, 51, 2901-2922.

Les, D. H., Crawford, D. J., Kimball, R. T., Moody, M. L., Landolt, E. 2003. Biogeography of discontinuously distributed hydrophytes: A molecular appraisal of intercontinental disjunctions. *Int. J. Plant Sci.,* 164, 917-932.

Luckenbach, M. W., Orth R. J., 1999. Interactions between benthic infauna and the transport and burial of Zostera marina seeds. *Aquatic Bot.*, 62, 235-247.

Lyons, A., P, Fox, W. L. J., Hasiotis, T. Pouliquen, E. 2002. Characterization of the two-dimensional roughness of wave-rippled sea floors using digital photogrammetry. *IEEE J. Ocean. Eng.*, 27, 515-524.

Lyons, A. P., Pouliquen, E., 2004. Advances in high resolution seafloor characterization in support of high-frequency underwater acoustics studies: techniques and examples. *Meas. Sci. Technol.*, 15, 59-72.

Marion, S. R., Orth, R. J., 2010. Innovative techniques for large-scale seagrass restoration using *Zostera marina* (eelgrass) seeds. *Rest. Ecol.,* 18, 514-526.

McGlathery, K. J., Sundback, K., Anderson, I. C., 2007. Eutrophication in shallow coastal bays and lagoons: The role of plants in the coastal filter. *Mar. Ecol. Prog. Ser.*, 348, 1-18.

McMahon, K., van Dijk, K., Ruiz-Montoya, L., Kendrick, G. A., Krauss, S. L., Waycott, M., Verduin, J., Lowe, R., Statton, J., Brown, E., Duarte, C., 2014. The movement ecology of seagrasses. *Proc. R. Soc. B*, 281, 20140878.

Nelson, J. M., Smith, J. D., 1989. Mechanics of flow over ripples and dunes. *J. Geophys. Res.*, 94, 8146-8162.

Munro, D. S., 1989. Surface roughness and bulk heat transfer on a glacier; comparison with eddy correlation. *J. Glaciol.*, 35, 343-348.

Olsen et al. 2004. North Atlantic phylogeography and large-scale population differentiation of the seagrass *Zostera marina L*. *Mol. Ecol.*, 13, 1923-1941.

Orth, R. J., Luckenbach, M., Moore, K. A., 1994. Seed dispersal in a marine macrophyte: implications for colonization and restoration. *Ecology*, 75, 1927-1939.

Orth, R. J., Harwell, M. C., Bailey, E. M., Barthlomew, A., Jawad, J. T., Lombana, A. V., Moore, K. A., Rhode, J. M., Woods, H. E., 2000. A review of issues in seagrass seed dormancy and germination: implications for conservation and restoration. *Mar. Ecol. Prog. Ser.*, 200, 277-288.

Orth, R. J., Carruthers, T. J., B., Denninson, W. C., Duarte, C. M., Fourqurean, J. W., Heck Jr., K. L., *et al.* 2006a. A global crisis for seagrass ecosystems. *Bioscience*, 56, 986-987.

Orth, J. R., Harwell, M. C., Inglis, G. J., 2006b. Ecology of seagrass seeds and seagrass dispersal processes. In: *Seagrasses: Biology, ecology and conservation*, eds. Larkum, A. W. D., Orth, R. J., Duarte, C. M. Springer, The Netherlands, pp. 111-133.

Orth, R. J., Luckenbach, M. L., Marion, S. R., Moore, K. A., Wilcox, D. J., 2006c. Seagrass recovery in the Delmarva Coastal Bays, USA. *Aquat. Bot.*, 90, 204-208.

Pereda-Briones, L., Infantes, E., Orfila, A., Tomas, F., Terrados, J., 2018. Dispersal of seagrass propagules: interaction between hydrodynamics and substratum type. *Mar. Ecol. Prog. Ser.*, 593, 47-59.

Pickerell, C. H., Schott, S., Wyllie-Echevarria, S., 2005. Buoy deployed seeding: demonstration of a new eelgrass (*Zostera marina L.*) planting method. *Ecol. Eng.*, 25, 127-136.

Raupach, M. R., 1992. Drag and drag partition on rough surfaces. *Bound.-Lay. Meteorol.*, 5, 285-308.

Raupach, M.R., Gillette, D.A., Leys, J. F., 1993. The effect of roughness elements on wind erosion threshold. *J. Geophys. Res.*, 98, 3023-3029.

Rees, W. G., Arnold, N. S., 2006. Scale-dependent roughness of a glacier surface: implications for radar backscatter and aerodynamic roughness modelling. *J. Glaciol.*, 46, 445-452.

Rhebergen, R., Cockburn, B., Jaap, J. W. van der Vegt, 2013. A space-time discontinuous Galerkin method for incompressible Navier-Stokes equations, *J. Comp. Phys.*, 233, 339–358.

Robert A., 1991. Fractal properties of simulated bed profiles in coarse-grained channels. *Math. Geol.*, 23, 367-382.

Ruiz-Montoya, L., Lowe, R. J., Van Niel, K. P., Kendrick, G. A., 2012. The role of hydrodynamics on seed dispersal in seagrasses. *Limmol. Oceanogr.*, 57, 1257-1265.

Short, F. T., Moore, K. A., 2006. Zostera: Biology, ecology and management In: *Seagrasses: Biology, ecology and conservation*, eds. Larkum, A. W. D., Orth, R. J., Duarte, C. M. Springer, The Netherlands, pp. 361-386.

Smith, M. W., 2014. Roughness in earth science. Earth-Sciences Rev., 136, 202-225.

Taylor, C., Hood, P., 1973. A numerical solution of the Navier-Stokes equations using the finite element technique. *Comput. Fluids*, 1, 73-100.

Ternat, F., Boyer, P., Anselmet, F., Amielh, M., 2008. Erosion threshold of saturated natural cohesive sediments: Modeling and experiments. *Water Resour. Res.*, 44, W11434.

Waycott et al. 1999. Accelerating loss of seagrasses across the globe threatens coastal ecosystems. *Proc. Natl. Acad. Sci. USA*, 106, 12377-12381.

Wiberg, P. L., Harris, C. K., 1994. Ripple geometry in wave-dominated environments. *J. Geophys. Res.*, 99, 775-789.

Wilcox, D.C. (1993), *Turbulence modeling for CFD*. DCW Industries Inc., California, 460 pp.

Xu, T., Moore, I. D., Gallant, J. C., 1993. Fractals, fractal dimension and landscapes: a review. *Geomorphology*, 8, 245-262.

Zarnoch, C. B., Hoellein, T. J., Bradley, T. F., Bradley, J. P. 2017. Eelgrass meadows, *Zostera marina* (L.), facilitate the ecosystem service of nitrogen removal during simulated nutrient pulses in Shinnecock Bay, New York, USA. *Mar. Poll. Bull.*, 124, 376-387.

## Figure Captions

**Figure 1.** Random realizations of micro-topographic transects for different Hurst exponents.

**Figure 2.** Finite element grid for a given micro-topography. The scope of the figure is intended to provide an understanding of the resolution of the mesh.

**Figure 3.** Scatter plot (grey dots) of the relationship between $U^+$ and $y^+$ obtained in the numerical simulation of a flow with free stream velocity $U_o$=0.2 m/s over a smooth surface. Black solid lines represent the theoretical relationship for different values of $y^+$.

**Figure 4.** Comparison between the theoretical and numerical vertical profiles of $U^+$ in the station at the middle of the test section (circles) and at the inflow boundary (triangles).

**Figure 5.** Scatter plot of the numerical relationship found between $<L_S>$ and $l^*\text{In}(U_o/U_c)$. Each circle (triangle) represents the ensemble average of $L_S$ over 10 random realizations with a given H and $U_o$ for the case of *Z. marina* (*P. oceanica*). Error bars correspond to the standard deviation in the ensemble. The grey straight line shows the best linear fit of the all data points.

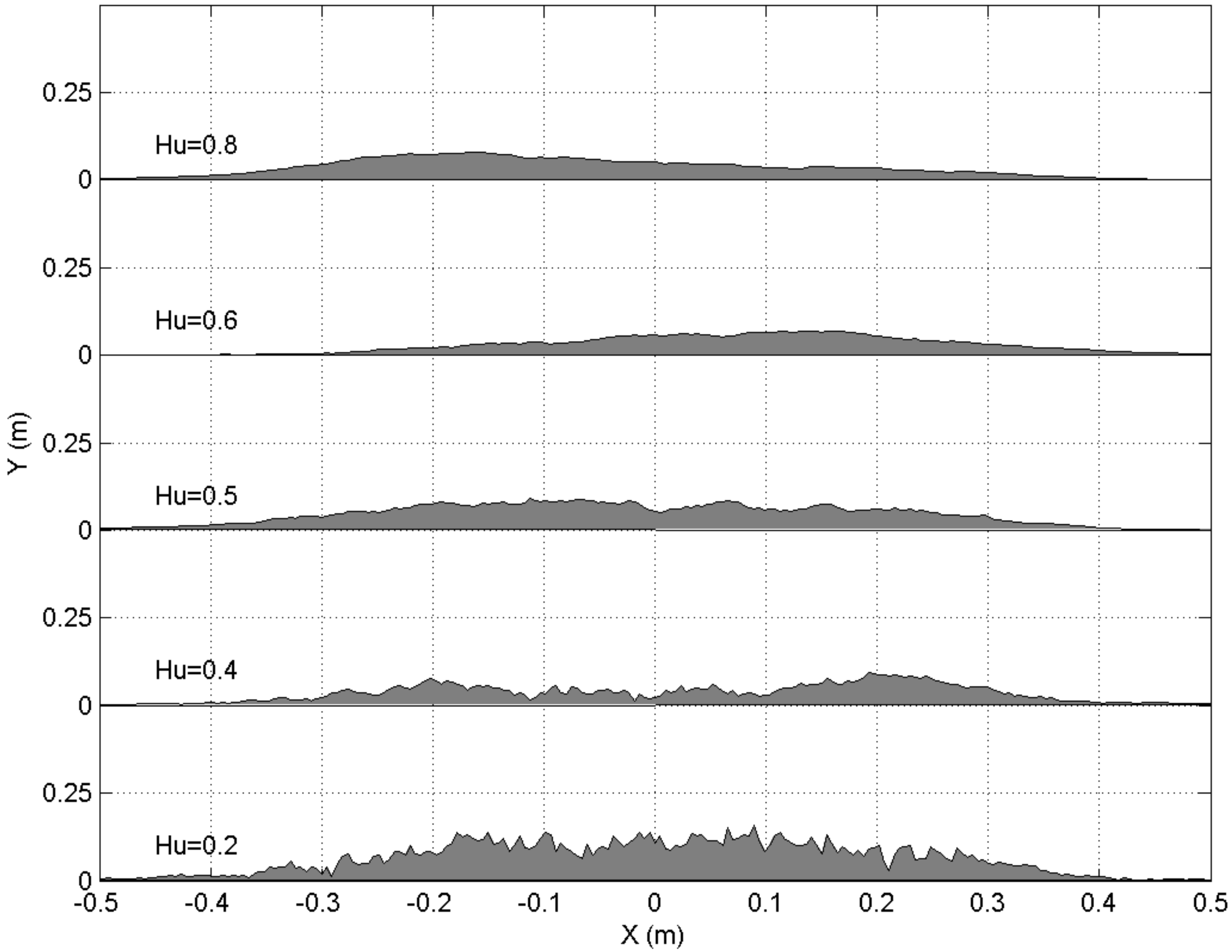

0.25
Hu=0.8
0
0.25
Hu=0.6
0
0.25
Hu=0.5
0
0.25
Hu=0.4
0
0.25
Hu=0.2
0
Y (m)
-0.5
-0.4
-0.3
-0.2
-0.1
0
0.1
0.2
0.3
0.4
0.5
X (m)


590 **Figure 1**

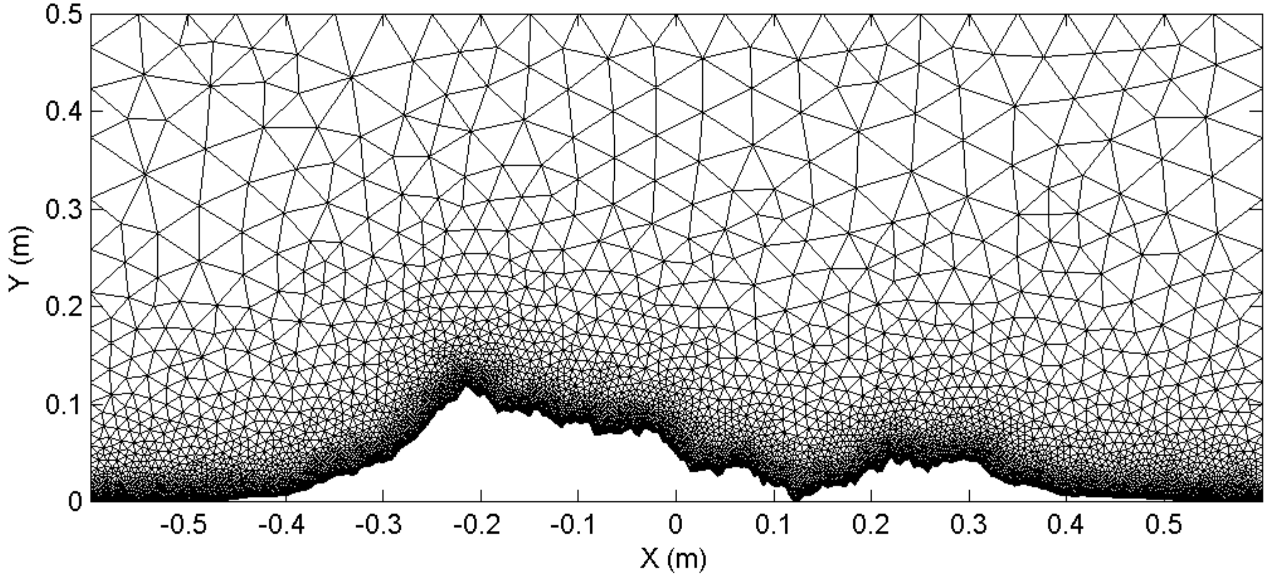


591 **Figure 2**

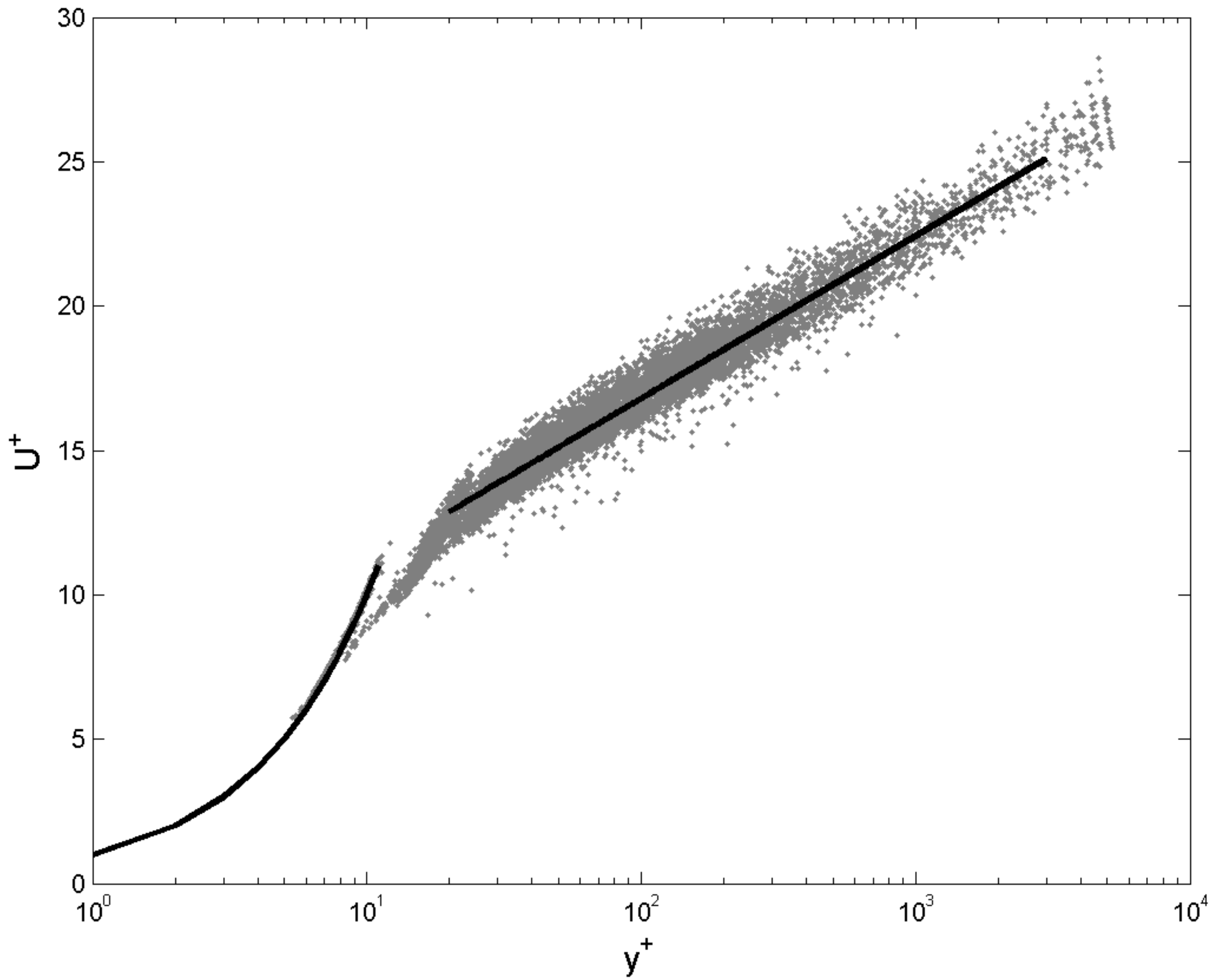


592 **Figure 3**

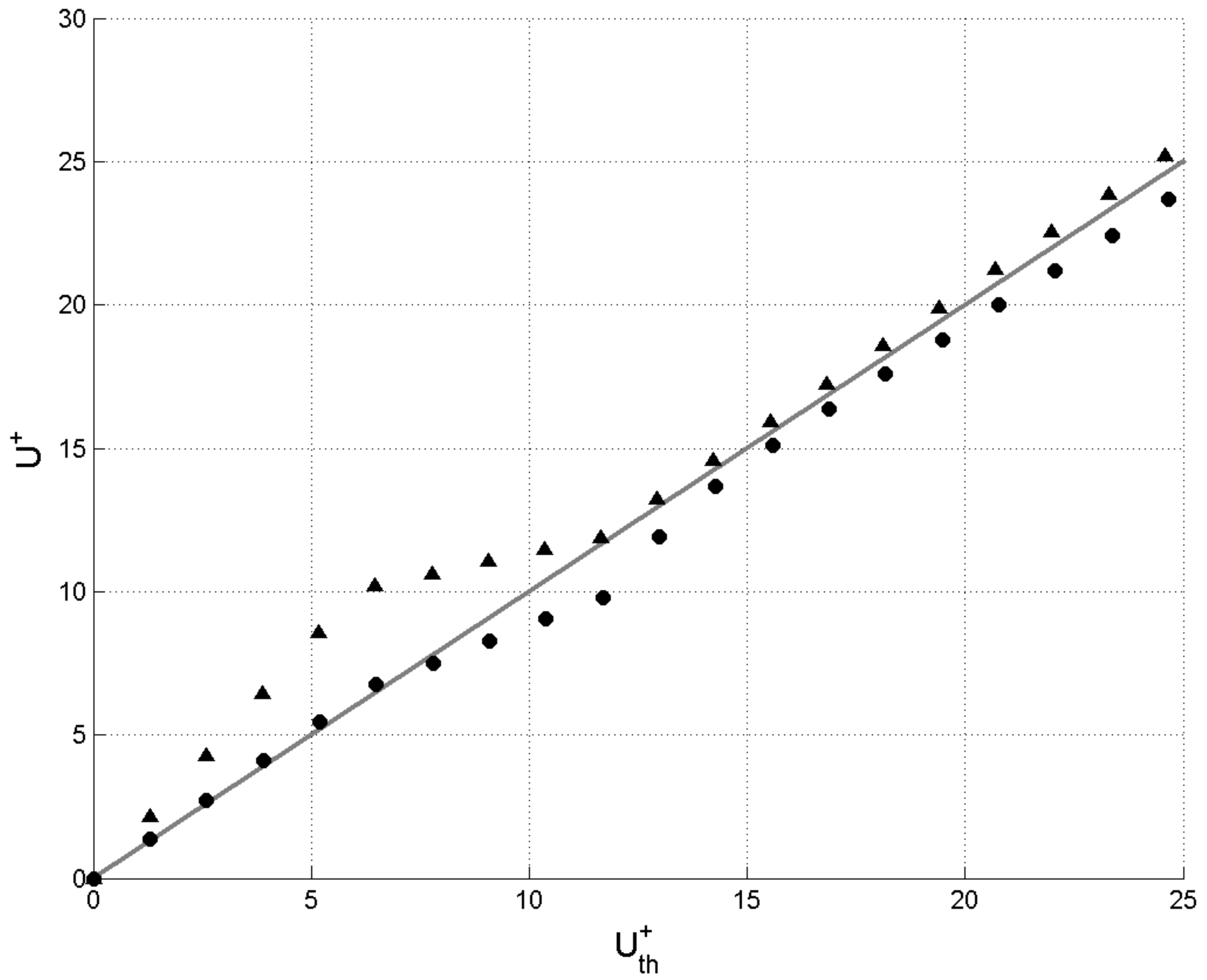


593 **Figure 4**

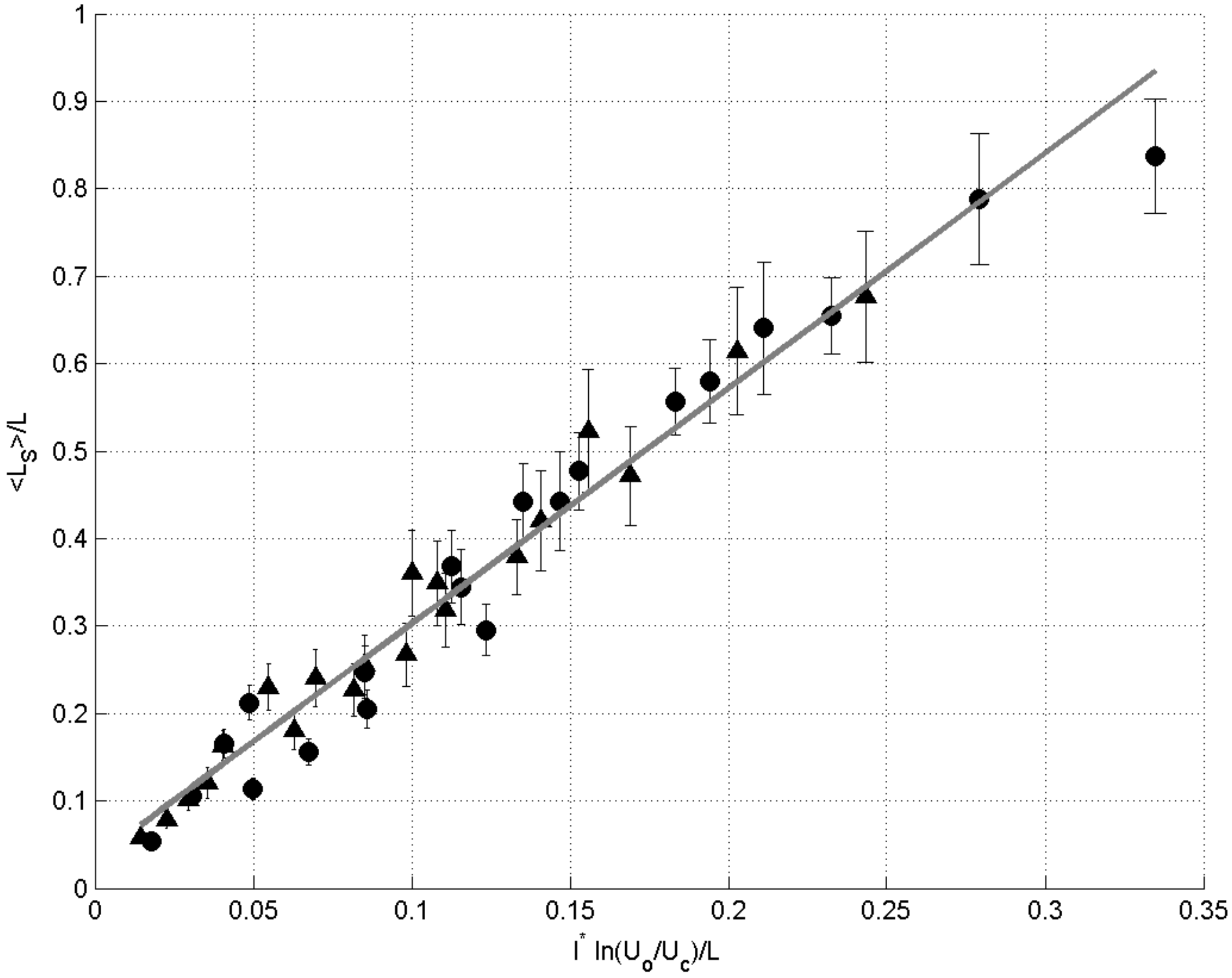

1
0.9
0.8
0.7
0.6
0.5
0.4
0.3
0.2
0.1
0
0
0.05
0.1
0.15
0.2
0.25
0.3
0.35
<L_S>/L
l* ln(U_o/U_c)/L


594 **Figure 5**

## Appendix 1: The Baldwin-Lomax eddy viscosity model

The Baldwin-Lomax eddy viscosity model, the most widely used algebraic model, assumes a two-layer concept wherein the boundary layer is split into inner and outer regions. Each layer is characterized by different turbulent length and velocity scales. The eddy viscosity in the outer region is formulated by the relation (Baldwin and Lomax, 1978; Wilcox, 1993):

$$[\nu_T]_{outer} = \alpha C_{cp} F_{wake} F_{kleb} \quad \text{(A.1)}$$

With the closure coefficients α=0.0168 and $C_{cp}$=1.6. The outer function $F_{wake}$ is:

$$F_{wake} = min\left(Y_{max} F_{max}, C_{wk} Y_{max} \frac{U_{dif}^2}{F_{max}}\right) \quad \text{(A.2)}$$

Where $C_{wk}$ =0.25 and $U_{dif}$ is the difference between the maximum and minimum velocities in the profile. $F_{max}$=max(yΩD) with Ω being the magnitude of the local time averaged vorticity and $D = \left(1 - e^{\frac{y^+}{A^+}}\right)$ is the Van-Driest damping factor ($A^+$=26 and $y^+$ = y $u^*$/ν, is the dimensionless distance from the wall in wall coordinates). $Y_{max}$ is the value of *y* where $F_{max}$ occurs. The Klebanoff intermittency factor $F_{kleb}$ is given by:

$$F_{kleb} = \frac{1}{1+5.5\left(C_{kleb} \frac{y}{Y_{max}}\right)^6} \quad \text{(A.3)}$$

With $C_{kleb}$=0.3. For the inner region, the eddy viscosity is given by the Prandtl-Van Driest formulation:

$$[\nu_T]_{inner} = (KyD)^2|\omega| \quad (A.4)$$

Where K=0.4 is the von Karman's constant and $|\omega|$ is the magnitude of the local vorticity. The boundary of the outer and inner layers is established at each streamwise station by the smallest value of y where $[\nu_T]_{outer}$ and $[\nu_T]_{inner}$ are equal.